Pattern Recognition 133 (2023) 109031

Contents lists available at ScienceDirect

Pattern Recognition

journal homepage: www.elsevier.com/locate/patcog

Transformed domain convolutional neural network for Alzheimer's disease diagnosis using structural MRI

S. Qasim Abbas [a], Lianhua Chi [a,**], Yi-Ping Phoebe Chen [a,*]

[a] Department of Computer Science and Information Technology, La Trobe University, Melbourne, VIC 3086 Australia

ARTICLE INFO

Article history:
Received 11 April 2022
Revised 19 August 2022
Accepted 5 September 2022
Available online 7 September 2022

Keywords:
Alzheimer disease (AD) detection
Brain disease
Convolutional neural network (CNN)
Supervised learning
Structural magnetic resonance imaging (sMRI)
Transform domain AD classification
AD diagnosis

ABSTRACT

Structural magnetic resonance imaging (sMRI) has become a prevalent and potent imaging modality for the computer-aided diagnosis (CAD) of neurological diseases like dementia. Recently, a handful of deep learning techniques such as convolutional neural networks (CNNs) have been proposed to diagnose Alzheimer's disease (AD) by learning the atrophy patterns available in sMRIs. Although CNN-based techniques have demonstrated superior performance and characteristics compared to conventional learning-based classifiers, their diagnostic performance still needs to be improved for reliable classification results. The drawback of current CNN-based approaches is the requirement to locate discriminative landmark (LM) locations by identifying regions of interest (ROIs) in sMRIs, thus the performance of the whole framework is highly influenced by the LM detection step. To overcome this issue, we propose a novel three-dimensional Jacobian domain convolutional neural network (JD-CNN) to diagnose AD subjects and achieve excellent classification performance without the involvement of the LM detection framework. We train the proposed JD-CNN model on the basis of features generated by transforming the sMRI from the spatial domain to the Jacobian domain. The proposed JD-CNN is evaluated on baseline T1-weighted sMRI data collected from 154 healthy control (HC) and 84 Alzheimer's disease (AD) subjects in the Alzheimer's disease neuroimaging initiative (ADNI) database. The proposed JD-CNN exhibits superior classification performance to previously reported state-of-the-art techniques.

1. Introduction

Alzheimer's disease (AD) is one of the most common type of neurodegenerative dementia that primarily impairs the function of brain neurons and its subsequent progression hampers cognitive reasoning [1]. It is reported that 5.8 million Americans were living with AD in 2019 and its prevalence has increased by 145% from 2000 to 2017 [1]. On a global scale, it has affected millions of people worldwide and the number of affected patients is expected to increase in the future. Early AD detection is often associated with amnesiac symptoms, but the quickest way to diagnose AD at the earliest stage is to measure brain atrophy, as amnesiac symptoms appear after brain cell atrophy has already occurred [2]. Successful early diagnostic assessments enable experts to adopt appropriate procedures in the initial stages of the disease which results in effective medication trials [1]. The earliest stage symptoms include deterioration in analytical skills and memory [1]. During this early stage, the atrophic process starts to affect the brain's neuron structure which ultimately leads to fully developed AD [3]. Many non-invasive measures, like structural magnetic resonance imaging (sMRI), functional magnetic resonance imaging (fMRI) and positron emission tomography (PET) etc., are available for AD diagnosis [4]. sMRI is quite popular among these available measures because it exhibits exceptionally high tissue contrast and excellent spatial resolution, which results in identifying minute structural changes associated with brain cells to detect AD and its prodromal stages with the help of computer-aided diagnosis (CAD) [5].

To quantify the structural changes in sMRI related to AD subjects, it is necessary to analyze variations in the structure of diseased brain tissue. These variations are quantified using conventional learning-based (CLB) and deep learning-based (DLB) techniques. CLB techniques normally extract handcrafted features such as gray matter (GM), white matter (WM), cerebrospinal fluid (CSF), cortical thickness and volume changes from sMRI data and employ them to train support vector machines (SVMs) or machine learning algorithms like random forest and linear SVM. The drawback of these techniques is the lack of coordination between features and the selected classifier, resulting in the degraded performance of the classification algorithms [6]. Recently, DLB techniques have

* Corresponding author.
** Co-corresponding author.
E-mail addresses: L.Chi@latrobe.edu.au (L. Chi), Phoebe.Chen@latrobe.edu.au (Y.-P.P. Chen).

https://doi.org/10.1016/j.patcog.2022.109031
0031-3203/

demonstrated superior performance in AD/HC classification tasks by incorporating powerful convolutional neural networks (CNNs), which have demonstrated great success in image classification.

The drawback of current CNN-based approaches is the requirement to locate discriminative landmark (LM) locations by identifying regions of interest (ROIs) or biomarkers [7] in sMRIs, thus the performance of the whole framework is highly influenced by the LM detection step. A wrongly detected LM may put the whole classification algorithm in jeopardy. The lack of a relationship between LM detection and classifier construction is also one of the hinderances in demonstrating the high performance of AD classification schemes. In addition, the LM detection step requires domain knowledge which is not available most of the time. To overcome these challenges, we propose a whole brain subject-level AD classifier with high performance characteristics.

In this paper, we propose a novel DLB framework that feeds whole brain Jacobian domain features at the subject-level to CNN to diagnose AD subjects, which neither identify any ROI region nor extract any 3D brain patches for classification. The proposed algorithm is a stepping-stone to accomplish CAD-based AD classification and autonomous diagnosis.

The proposed novel *Jacobian domain convolutional neural network* (JD-CNN) framework consists of three broad stages, namely: (i) preprocessing; (ii) Jacobian map generation; and (iii) the CNN. The standard pre-processing operation involves four sub-steps, namely: (i) anterior commissure (AC) posterior commissure (PC) alignment correction, (ii) intensity correction, (iii) skull stripping and (iv) image registration. Further, the pre-processed images are utilized to compute the Jacobian determinant maps, which provides a quantitative measure to identify the atrophy patterns associated with AD. The Jacobian domain (JD) transformation computes linear approximation of brain matter at each voxel of sMRI. First, a 3D Jacobian matrix is computed from 3D spatial domain (SD) sMRI. This Jacobian matrix is then employed to calculate a Jacobian determinant at each voxel and the new resultant matrix is called the Jacobian map. One of the characteristics of the Jacobian map is to provide a volumetric ratio of approximate localized atrophy patterns to the original un-atrophy pattern available in SD images and hence the measure of volumetric change is recorded [8]. Consequently, when there is no localized volumetric change in an SD image then the corresponding voxel values in the JD image are equal to unity and vice versa. In this way, the analysis of the JD image reveals the localized anatomical brain degeneration patterns due to volumetric changes in sMRI of AD subjects [9]. Ye et al. [10] have also employed Jacobian determinants to track localized myocardium motion for quantification the motion field. We demonstrate the supremacy of JD features over SD features for AD/HC classification in this work. The JD maps are subsequently exploited to train the CNN classifier, while the trained CNN classifier provides AD vs. HC classification. In the experiments, the training, validation and testing of the JD-CNN is performed on the sMRI data collected from the ADNI database [11]. The experiment results show the superior performance of the proposed algorithm against previously reported state-of-the-art classification schemes. Following are the main contributions of this paper.

- We propose a novel JD-CNN architecture which exploits the JD features to train a three-dimensional CNN for AD classification. The CNN training in JD improves the efficiency of CNN features to increase the classification performance because the JD inherently captures the localized volumetric transitions at the voxel level, which is key to identify sMRI patterns associated with AD.
- We study the effect of JD features over classifier performance.
- We develop a classifier which does not require any discriminative landmark detection and extraction strategy, resulting in the reduced computational complexity of the classification framework.

The remainder of the paper is organized as follows. In Section II, a concise review of the previously reported AD classification algorithms employing sMRI is presented. In Section III, the demographics of the studied material and the adopted preprocessing pipeline for homogenizing the dataset is elaborated. Section IV describes the methodology to generate Jacobian features and the proposed CNN architecture. In Section V, the performance of the proposed JD-CNN is evaluated and compared with state-of-the-art algorithms. Section VI describes the differences between the proposed JD-CNN and the previously reported algorithms for AD vs. HC classification, and finally Section VII concludes the paper.

Algorithm 1, Algorithm 2

2. Related work

In this section, a concise description of the existing sMRI-based classification schemes is provided. The previous studies are divided into two broad categories: namely conventional learning-based (CLB) and deep learning-based (DLB) techniques.

2.1. Conventional learning-based techniques (CLB)

Traditionally, CLB technique features are generated by quantifying structural changes linked with the brain's density maps, surface area and regions [12]. Typically, density map-based approaches employ gray matter (GM), white matter (WM), cerebrospinal fluid (CSF), cortical thickness, volume change or a combination of any of these to quantify changes in the brain's structure associated with atrophic process due to the progression of AD. Usually, the GM, WM and CSF maps are generated by means of voxel-based morphometry (VBM). Moller et al. [13] proposed a VBM-based AD framework that classified AD patients by analyzing GM density maps and incorporating an SVM classifier. Normally, the VBM approaches suffer from the generalization problem due to high dimensional sMRI data with millions of voxels. To overcome the overfitting hurdle, dimensionality reduced density maps were generated for AD classification. Salvatore et al. [14] employed principle component analysis (PCA) for dimensionality reduced WM and GM density maps. Due to the classifier's over-dependence in the dimensionality reduction step, it may be a bottleneck in developing VBM-based high-performance classifiers.

Surface area-based approaches exploit alterations in the brain's temporal and parietal regions of the cortical surface. In any classification framework, the surface area plays the same role as the localized volumetric data in the density map. Li et al. [15] computed cortical surface morphological features from all vertices to develop an SVM-based classifier. The high-dimensional surface area-based approaches suffer from a similar generalization problem as density map-based classifiers and these types of algorithms also require dimensionality reduction approach to avoid overfitting. Park et al. [16] proposed an SVM-based AD classifier by adopting cortical thickness and sulcal depth in terms of three dimensional meshes which employed PCA-based dimensionality reduction mechanism.

Region-based approaches take advantage of the features generated from specific brain regions. The brain regions are either pre-defined based on histological prior studies or anatomical brain atlases. Liu et al. [17] proposed a relationship-induced multi-template learning method such that every single image in the dataset is non-linearly registered onto multiple pre-selected atlases using spatial normalization to extract regional features. These features are subsequently utilized to develop ensemble classifiers for AD diagnostics. These types of techniques have a degraded performance possibly due to heterogeneities between the generated fea-

Algorithm 1
Pre-processing operations to homogenize dataset.

Input: Input image I from ADNI-1 database.

Output: G_{AT} (affine registered image).
1: **FOR** $i = 0$ to N **do** // N is the total number of selected images for this study
2: Compute a flipped version (F) of input image (I); //ACPC correction starts here
3: Determine MSP of I using equation (2) in such a way that equation (1) yields maximum symmetric image plane;
4: Transform I to PIL orientation;
5: Identify AC and PC positions of I using pretrained model;
6: Apply rigid transformation to correctly align ACPC line;
7: Inverse transform I from PIL orientation;
8: Shift image intensity from T_m to T_{new}. Intensity correction; //Intensity correction starts here
9: Distribute all intensities around T_{new} by ensuring $\sigma = 1$;
10: Fit intensity corrected image over a standard template SRI24 to calculate R_f transformation and I_{RA}; //Skull stripping starts here
11: I_{RA} is segmented into GM, WM, and CSF;
12: Fuse the generated GM, WM and CSF segments of to get I_{AM};
13: Map I_{AM} to I_{RA} for generating skull stripped image;
14: Map skull stripped image to standard Colin27 template; //Image registration starts here
15: Generate G_{AT} using equation (3);
16: **END**

Algorithm 2
Proposed JD-CNN.

Input: G_{AT} (affine registered images).

Output: Predicted binary class labels $\hat{y}$.
1: **FOR** $p = 0$ to N **do** // N is the total number of G_{AT} images
2: Initialize a null matrix $\boldsymbol{J_f}$ having dimensions 181 × 217 × 181 to store Jacobian map corresponding to G_{AT}.
3: **FOR** $q = 0$ to V_{AT} **do** // V_{AT} is the total number of voxels in G_{AT}
4: $\boldsymbol{J_v} \leftarrow \nabla \boldsymbol{v}(I(i_q,\ j_q, k_q)_{G_{AT}})$ // using equation (4)
5: $|\boldsymbol{J_v}| \leftarrow \det(\boldsymbol{J_v})$ // using equation (5)
6: $\boldsymbol{J_f} \leftarrow \boldsymbol{J_f} \cup |\boldsymbol{J_v}|$ // store $|\boldsymbol{J_v}|$ scalar value to 3D $\boldsymbol{J_f}$ matrix
7: **END**
8: **END**
9: Initialize *Sequential* model, three convolutional, three max-pooling, a flatten, a fully connected and an output layer.
10: **FOR** $r = 0$ to N **do**
11: $\boldsymbol{C_{1st}} = \{\boldsymbol{C}_1,\ \boldsymbol{C}_2,\ \ldots,\ \boldsymbol{C}_{16}\} \overset{3\times3\times3}{\leftarrow} conv3D_{1st}\ (\boldsymbol{J_f})$ //where $C_i \in \mathrm{R}^{w\times w\times w}$ and params #448
12: $\boldsymbol{MP_{1st}} \overset{3\times3\times3}{\leftarrow} max\text{-}\ pooling(\boldsymbol{C_{1st}})$
13: $\boldsymbol{C_{2nd}} = \{\boldsymbol{C}_1,\ \boldsymbol{C}_2,\ \ldots,\ \boldsymbol{C}_{32}\} \overset{5\times5\times5}{\leftarrow} conv3D_{2nd}(\boldsymbol{MP_{1st}})$ // Params #64,032
14: $\boldsymbol{MP_{2nd}} \overset{4\times4\times4}{\leftarrow} max\text{-}\ pooling(\boldsymbol{C_{2nd}})$
15: $\boldsymbol{C_{3rd}} = \{\boldsymbol{C}_1,\ \boldsymbol{C}_2,\ \ldots,\ \boldsymbol{C}_{64}\} \overset{7\times7\times7}{\leftarrow} conv3D_{3rd}(\boldsymbol{MP_{2nd}})$ // Params #702,528
16: $\boldsymbol{MP_{3rd}} \overset{5\times5\times5}{\leftarrow} max\text{-}\ pooling(\boldsymbol{C_{3rd}})$
17: $\boldsymbol{FD} \overset{3D\ to\ 1D}{\leftarrow} flatten\ data(\boldsymbol{MP_{3rd}})$
18: $\boldsymbol{D} = \{\boldsymbol{D}_1,\ \boldsymbol{D}_2,\ \ldots,\ \boldsymbol{D}_{16}\} \leftarrow dense(\boldsymbol{FD})$ // Params #2064
19: $\hat{y} \leftarrow \varsigma(\boldsymbol{D})$ // Params #34
20: **END**

tures and adopted classifiers. Another possible reason for demonstrating sub-optimal learning performance is that the hand-crafted features generated from sMRIs to build suitable classifiers do not coordinate well with the classification framework [18]. Hence, deep learning-based approaches emerge to help achieve superior classification performance due to the unification of the hand feature extraction stage and corresponding classifier.

2.2. Deep learning-based techniques (DLB)

Recently, numerous deep learning-based (DLB) techniques (specifically CNNs) have been proposed to classify AD affected subjects. The deep CNNs are employed to generate the feature space for disease classification. Three-dimensional (3D) DLB classifiers are divided into the following three categories, depending on the nature of the employed features: (i) patch-based, (ii) ROI-based, (iii) subject-based.

Patch-based DLB approaches extract 3D patches from sMRIs [19]. Lian et al. [20] proposed a patch-level classifier that automatically extracts image patches around the LM locations available in sMRI data by exploiting a weakly-supervised learning methodology and then computing group comparisons between HC and AD samples to train their ensemble network. Their framework employed non-linear registration to build voxel-wise anatomical correspondence between different subjects, which is computationally expensive and a hinderance in developing a time efficient classifier. Liu et al. [21] demonstrated the efficiency of a landmark-based CNN technique by extracting image patches around predefined landmark locations. These image patches are then utilized to train a CNN model. The drawback of their technique is that each DenseNet is independently trained and hence it is challenging to optimize the complete framework. The main limitation of patch-level DLB frameworks is their complexity. In these approaches, normally each patch is independently input to train sub-networks, called patch-level sub-networks. The outputs from these patch-level sub-networks are subsequently fused and retrained at region-level and subject-level sub-networks respectively [19].

ROI-based approaches extricate 3D patches only from the specific informative brain parts, unlike patch-based algorithms which slice whole or LM identified brain parts into patches. The rationale of employing the ROI-based approach is that all patches extracted through patch-based schemes do not necessarily contain atrophy patterns and hence their selection is not worthwhile [19]. Normally, the ROI-based classifiers focus on those brain parts which have demonstrated comparatively higher levels of atrophic degradations due to the progression of AD, resulting in maximizing the

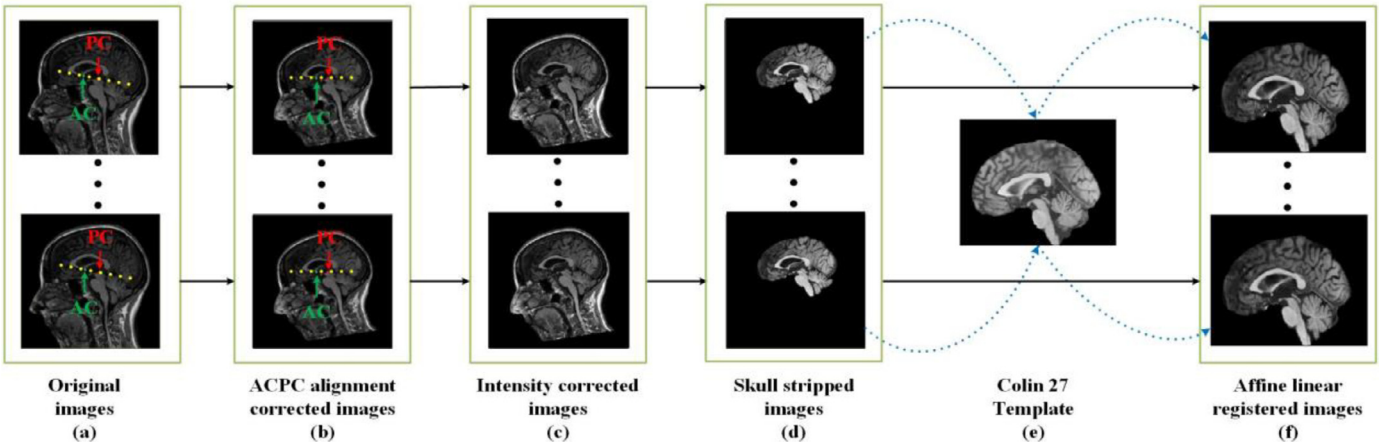

Fig. 1. Illustration of pre-processing operations to homogenize the dataset. (a) Original image with misaligned ACPC line (indicated by dotted yellow line). (b) Orientation corrected version with horizontal ACPC line. (c) Effect of intensity correction. (d) Extraction of brain tissue. (e) A skull stripped Colin27 template for image registration. (f) Affine linear registered image after removing global inconsistencies.

group difference between AD and HC. Typically, the ROIs are selected on a priori basis. Another advantage of the ROI-based approaches is the reduction in the complexity of the framework due to fewer volumetric ROI-based patches. Lin et al. [22] proposed a hippocampus-based classification framework, which performed a deformable registration of hippocampus as part of the image processing block to link voxel-wise correspondence between different entities and then extracted 151 patches from each image for inputting to the classifier. The chief drawback of these frameworks is the selection of only a specific or a handful of ROIs to identify AD patterns, while the atrophic process occurs in the entire brain and not just in some specific isolated brain regions. Another limitation of this approach is the identification of localized discriminative brain regions in the sMRI before training any network/model, which affects the performance of the classification framework and eventually, the diagnostics becomes unreliable.

Both the patch-based and ROI-based classification frameworks lack whole-brain spatially-correlated information. To overcome this limitation, a subject-based framework [23, 24] is designed which takes the whole-brain image as input at once. This type of framework performs subject-level classification. Wang et al. [23] reported an ensemble whole-brain classification framework with the help of 3D CNN layers. The framework included dense blocks between CNN layers to maximize the information flow. Basaia et al. [24] proposed a classifier without any feature engineering and its performance was not affected by heterogeneities in the imaging scanner. The details of the adopted procedures and their corresponding parameters were not reported [24]. Wen et al. [19] analyzed the classifiers reported in [23, 24] and concluded the prevalence of data leakage in these frameworks. The data leakage phenomenon refers to any of the following four main concerns (i) wrong dataset split, (ii) late split, (iii) biased transfer learning and (iv) absence of an independent test set [19]. Lian et al. [25] developed an end-to-end DLB classifier for the joint regression of multiple clinical scores. The results were comparatively better but might not be precise enough for AD diagnosis.

The key concerns regarding subject-based DLB approaches is the lack of explanation about adopted preprocessing procedures and the prevalence of data leakage reported in [19], which hampers the diagnostic performance of unseen test datasets. The lack of a preprocessing explanation means the absence of motivation behind its adaptation or a lack of technical information due to its in-house development.

We developed a novel transformed domain whole-brain subject-level AD classification algorithm that may not have any data leakage. In addition, we provide a detailed explanation of the adopted preprocessing procedures for reproducible evaluation.

3. Preprocessing

Structural magnetic resonance imaging (sMRI) modality requires certain specific preprocessing operations before they can be utilized in a relevant classification algorithm for diagnostic purposes. We implemented a standard preprocessing pipeline to uniformize images across a complete dataset. The uniformization process is necessary to harmonize sMRIs across all dataset images.

We adopted four standardized pre-processing operations, namely: ACPC alignment correction for identical orientation, intensity correction for uniform homogeneity, skull stripping to extract brain tissue and image registration for geomatic alignment. The complete preprocessing flow diagram is shown in Fig. 1. We exploit *structural equation modeling (SEM) tools* available under the *Nipype* interface [26] for ACPC alignment and intensity correction, skull stripping is performed by employing *Insight Toolkit (ITK)* [27], while image registration is accomplished with the help of *advanced normalization tools (ANTs)* [28].

3.1. Dataset

The performance of the proposed JD-CNN algorithm is evaluated on baseline T1-weighted sMRI data collected from 154 healthy control (HC) and 84 AD subjects from an Alzheimer's disease neuroimaging initiative-1 (ADNI-1) database [11]. The images included in this study are captured by a scanner with a magnetic field strength of 3T, so the spatial and voxel resolutions are not uniform across all dataset images. The minimum and maximum spatial resolutions of the studied images are $240 \times 256 \times 160 and 256 \times 256 \times 170$ respectively, while the voxel resolutions are presented in Table S-I in the supplementary material.

The repetition time (TR) and echo time (TE) of the scanner during sMRIs acquisition are 6.802 ms and 3.158 ms respectively [11]. The selection of these specific images from the ADNI-1dataset is based on the following three conditions:

- Eyes in the MSP aligned image must be lower than the AC point in a superior-inferior direction.
- The physical distance between the left and right eye must be at least 40 mm.
- The non-zero norm for a bounding area which means that the algorithm doesn't converge, and the resulting ACPC points are not located precisely.

TABLE 1
Demographic information of 238 studied subjects from ADNI-1 database.

Category	Diagnostic group	Subject count	Gender(M/F)	Age (Years)	Education (Years)	MMSE	ADAS-11	DIGITSCOR
Training	HC	92	31/61	75.88 ± 03.99	15.95 ± 1.90	29.13 ± 0.75	06.18 ± 02.64	48.55 ± 09.12
	AD	51	15/36	73.49 ± 08.04	13.86 ± 2.46	21.42 ± 3.88	21.31 ± 08.15	27.01 ± 12.67
Validation	HC	31	13/18	75.25 ± 03.77	16.53 ± 1.52	29.28 ± 0.50	06.46 ± 02.46	51.41 ± 06.82
	AD	16	05/11	73.65 ± 09.25	15.18 ± 3.13	21.87 ± 3.61	19.25 ± 7.52	30.89 ± 13.40
Testing	HC	31	14/17	75.61 ± 03.95	16.07 ± 1.96	29.16 ± 0.73	06.18 ± 2.46	47.12 ± 09.89
	AD	17	07/10	73.55 ± 05.73	14.64 ± 3.14	21.05 ± 3.79	22.18 ± 6.74	26.99 ± 11.89

The division of subjects into HC and AD categories is based on standard clinical criteria, including the mini-mental state examination (MMSE) score, Alzheimer's disease assessment scale (ADAS-11) which includes 11 subject participation tasks and the digit symbol total correct (DIGITSCOR) score. We also ensure that all images of a subject are assigned to a single category and must not split to others, for example, if one image of a subject is assigned to the training category, then all other available images of that subject, which are taken at some other time frame, must also be assigned to the training category. In addition, we ensure that the duplicate sMRI samples must also be removed from the selected data.

The proposed model is trained, validated, and tested on a set of 143,47 and 48 images respectively. The selection of subjects in the specific diagnostic group is performed randomly. The demographic information of the 238 studied subjects from the ADNI database is reported in Table 1.

3.2. ACPC alignment correction

The AC and PC are both WM tracts that link the cerebral hemispheres of the brain. However, there is a potential alignment problem with the original dataset images. The obstacle is that the images are not oriented in an identically uniform manner, which affects the diagnosis efficiency of any classification scheme. To resolve this issue, Ardekani et al. proposed a two-stage methodology [29, 30] that corrects the orientation of 3-dimensional MRI images. The proposed scheme [29] tries to align the image into a maximum symmetric plane by calculating the cross-correlation between two halves of a single image. In the first stage, the algorithm takes the unoriented image (I) as input and mirrors this image across the plane to obtain a flipped version of I as F. The cross-correlation computational function $s(I, F)$ between I and F is represented by (1).

$$\boldsymbol{s(I,F)} = \frac{\sum_{\boldsymbol{i}}\sum_{\boldsymbol{j}}\sum_{\boldsymbol{k}}\left(\left(\boldsymbol{I_{ijk}}-\boldsymbol{\mu'}\right)\left(\boldsymbol{F_{ijk}}-\boldsymbol{\mu''}\right)\right)}{\sqrt{\sum_{\boldsymbol{i}}\sum_{\boldsymbol{j}}\sum_{\boldsymbol{k}}\left(\left(\boldsymbol{I_{ijk}}-\boldsymbol{\mu'}\right)^2\right)\sum_{\boldsymbol{i}}\sum_{\boldsymbol{j}}\sum_{\boldsymbol{k}}\left(\left(\boldsymbol{F_{ijk}}-\boldsymbol{\mu''}\right)^2\right)}} \tag{1}$$

where I is the original input image, μ' is the mean value of I, F is the flipped version of I and μ'' is the mean value of F, while i, j and k represent three dimensions of an MRI. Both the AC and PC locations normally lay over the mid-sagittal plane (MSP) and the MSP in the image is generically represented by Eq. (2) [30].

$$\boldsymbol{X_i} + \boldsymbol{Y_j} + \boldsymbol{Z_k} = 1 \tag{2}$$

where X_i, Y_j and Z_k represent a unique set of parameters to characterize a three-dimensional plane containing MSP. The three unknown factors X_i, Y_j and Z_k need to be calculated to correctly identify MSP and they are computed by optimizing Eq. (2) in such a way that Eq. (1) produces the maximum value to acquire the maximum symmetric plane [29]. Then, the images are transformed to a posterior-inferior-left (PIL) orientation by ensuring that MSP aligns along the $x = 0$ plane.

In the second stage, a model-based approach [30] is used where a model is trained with the already identified AC and PC locations. The dataset images are fed into the trained model to identify the approximate locations of the AC and PC points. Subsequently, a small number of perturbations in the form of translation and rotation are applied to align AC and PC locations along MSP. A linear rigid transform is utilized to ensure the ACPC line is parallel to the z-axis (i.e. posterior in PIL) of the input image, the subject's feet align to the y-axis (i.e. inferior in PIL), and the MSP aligns itself along the $x = 0$ plane. In an unaligned image, the straight line joining AC and PC locations make some angle (θ) with the z-plane (i.e. posterior in PIL and shown as the yellow dotted line in Fig. 1). The correctly aligned brain image in the PIL orientation forms an angle $\theta = 0^\circ$ with the posterior axis. In this way, all the dataset images are aligned with a uniform orientation. Finally, an inverse PIL transformation is calculated and applied to transform the image back to its original axis without changing its spatial resolution.

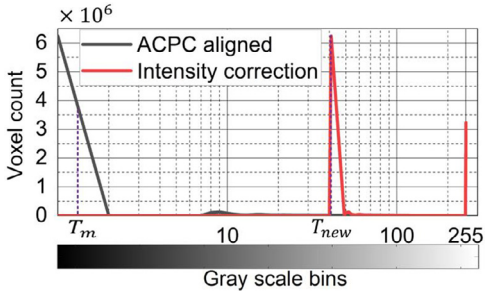

Fig. 2. Effect of intensity correction over the image histogram of an arbitrary HC sMRI. The black and red lines indicate the voxel distribution before and after intensity correction. The mean voxel value is shifted from T_m to T_{new} after homogenizing the intensity distribution.

3.3. Intensity correction

The MRI images do not exhibit uniform homogeneity across the whole dataset, and it changes evenly within an image. This non-uniformity contributes to variations in images and is quite negligible for visual inspection. This type of inconsistency in images does not contribute to any diagnoses challenge for domain experts but affects the performance of CAD significantly. To resolve this problem, intensity correction must be performed for each individual image to achieve uniform homogeneity across all images included in study. This step enables CAD frameworks to exhibit better classification performance.

MRI data suffers from image inhomogeneity and hence voxel values differ appreciably from one image to another with the same characteristics. To resolve this problem, image intensity distribution is rescaled for each sMRI of the dataset by shifting its mean intensity T_m to a new value T_{new} in such a way that the standard deviation σ comes out as unity without changing its spatial resolution. The effect of intensity rescaling is evident from Fig. 2 where the majority voxel values of the ACPC aligned image reside very close to the origin and the mean intensity of the ACPC corrected image is T_m, while after intensity rescaling, the mean intensity is

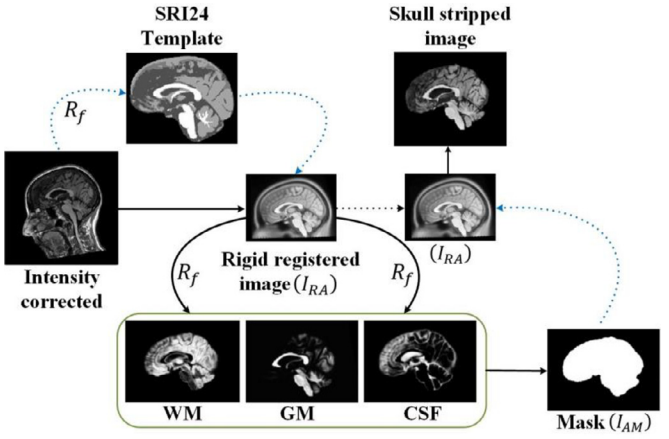

Fig. 3. Illustration of SRI24 template-based skull stripping, which strips non-brain tissue from the image.

shifted to T_{new} and all other intensities are distributed by ensuring $\sigma = 1$.

3.4. Skull stripping

The process of effectively segmenting brain tissue (cortex and cerebellum) from a non-brain structure (e.g. skull and eyeballs etc.) is called skull stripping. The resultant image contains only brain matter, while all non-brain matter is filtered out. This process helps all CAD frameworks to focus on the brain structure responsible for the AD while non-brain matter does not contribute any significance for diagnoses procedures.

An atlas-based skull stripping technique is used in this step which employs a standard SRI24 template image [31] to distinguish and separate brain tissue from non-brain tissue. SRI24 is an MRI-based atlas of normal adult human brain anatomy, generated by template-free nonrigid registration from images of 24 HC subjects [31]. The ages of all 24 subjects involved in template generation are different. As there are 24 different age groups, the adult brain template which is formed has more generality across all age groups. The youngest and oldest persons are aged 19 years and 84 years respectively [31]. The SRI24 atlas is generated from images acquired from a scanner with a magnetic field strength of 3T [31], and our studied dataset is also collected from a 3T scanner. Moreover, the 3T scanner exhibit improved tissue contrast compared to 1.5T, which results in an efficient skull stripping operation. Hence, the SRI24 atlas is preferred over other available atlases in this step.

The standard template is fitted over each intensity-corrected image to calculate a rigid registration function (R_f) and acquire a registered atlas version I_{RA} of the input sMRI. The R_f only allows rotation and translation operations, and is utilized for segmenting the image into GM, WM and CSF which are fused to produce an atlas mask I_{AM} for brain tissue. Then, the I_{AM} is mapped to I_{RA} to generate a skull stripped image. The complete skull stripping process is depicted in Fig. 3.

It is important to note that this step utilizes a template to identify brain tissues. This step must not be confused with the regions of interest (ROIs)-based approach, where specific ROIs (i.e. specific brain regions) are extracted from brain images and fed to the classifier, whereas we extract whole brain images and do not rely on any specific ROI.

3.5. Image registration

This step involves a 3-dimensional image registration by utilizing affine transformation (AT) which registers a skull stripped image to a skull stripped Colin27 template space [32] with a spatial resolution of 181 × 217 × 181 voxels. The procedure to perform skull stripping of a standard Colin27 template is the same as explained in section 3.4. In other words, the skull stripped Colin27 template is aligned to the SRI24 template space and the AT can only perform shearing and scaling operations. The Colin27 atlas is preferred in this step because it demonstrates an overlap score of 0.414 compared to SRI24's 0.412 for equally weighted AFFINE registration [31]. The higher overlap score motivates us to utilize the Colin27 atlas for spatial normalization.

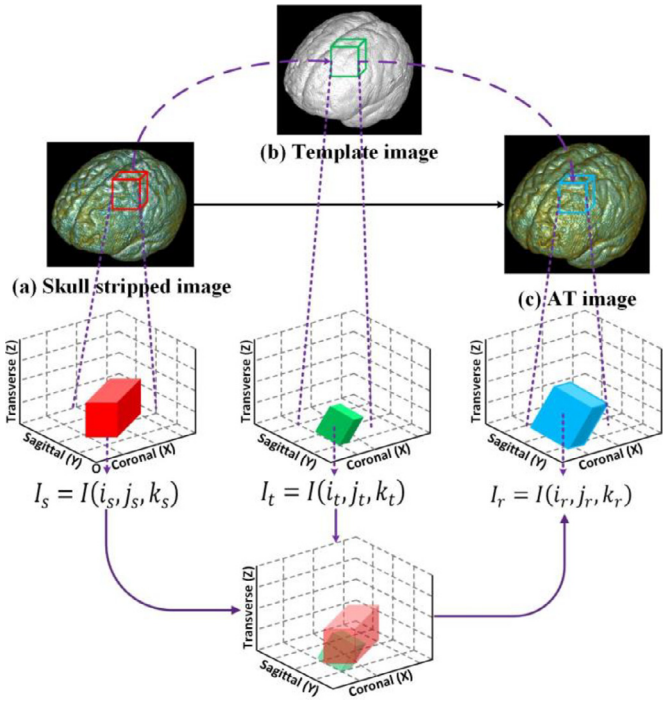

Fig. 4. Illustration of arbitrary voxel mapping from I_s to I_t for image registration to produce I_r with the help of the mattes cost function. (a) Skull stripped sMRI. (b) Standard Colin 27 template sMRI. (c) Affine linear registered sMRI. The red cube indicates the voxel before AT, the green cube indicates the corresponding template voxel and the blue cube indicates the registered version of the red voxel.

AT is a linear transformation that preserves the structure of the image space and induces only geometric distortions by transforming $D^s \rightarrow D^{ARS}$, where D^s and D^{ARS} both represent computational spatial domains before and after AT. Let $I_s = I(i_s, j_s, k_s)$ be the spatial domain value of one of the voxels v_s in the skull stripped image, $I_r = I(i_r, j_r, k_r)$ be its transformed value, and $I_t = I(i_t, j_t, k_t)$ be the value in the standard template space. This step transforms the position of I_s by changing its positional vectors from (i_s, j_s, k_s) to (i_r, j_r, k_r) according to (i_t, j_t, k_t) over a computational spatial domain D^s using mattes as a cost function and is represented by Eq. (3).

$$\boldsymbol{G_{AT} \in I_r | I_r : I_s \rightarrow I_t, \ \forall I_s \in D^s} \tag{3}$$

where G_{AT} is an AT image that contains all voxels of a skull stripped image in a new vector space (i_r, j_r, k_r). The affine transformed vector space (i_r, j_r, k_r) is in alignment with a standard template space (i_t, j_t, k_t) where $I(i_r, j_r, k_r) \in G_{AT} \rightarrow D^{ARS}$. The mapping of an arbitrary voxel I_s to I_t to acquire I_r is illustrated in Fig. 4.

Affine registration is utilized to remove scale anomalies across complete datasets by registering each image to a standard template. In addition, this process also changes the spatial resolution of images to 181 × 217 × 181 voxels as well as resamples all images to acquire uniform voxel resolution of $1 \times 1 \times 1\ mm^3$.

4. Proposed 3D Jacobian domain convolutional neural network

The pre-processed images are transformed to the Jacobian domain to generate a Jacobian determinant map, which is utilized to train a CNN model. Recently, Ye et al. [10] investigated the tracking of regional myocardium motion on cardiac tagging MRI scans. The authors utilized Jacobian determinant maps as evaluation metrics for quantifying the motion field orientation to measure its smoothness, perseverance and bijectivity through unsupervised deep learning. Stypułkowski et al. [33] employed Jacobian determinants to fulfill the tractability requirement of normalizing flows for developing a conditional flow-based point cloud generator. Spasov et al. [34] exploited Jacobian maps to develop a multimodal framework which quantified local volumetric transitions associated with AD. These studies [10, 33, 34] motivate us to take advantage of Jacobian determinant maps for quantifying voxel-level volumetric transitions associated with AD through a deep learning-based framework. The conversion of the image from the spatial domain to the Jacobian domain is performed using *ANTs* [28] through non-geometric parameter settings. The implementation details and the proposed architecture are explained in this section.

4.1. Feature extraction

The affine registered images G_{AT} from the previous pre-processed stage are used to generate Jacobian maps $|\boldsymbol{J_f}|$, which are subsequently utilized to train the proposed convolutional network. The $|\boldsymbol{J_f}|$ quantifies changes in the brain's volumetric tissue in an sMRI. These changes are key to monitoring the anatomical alterations in the brain's structure and transfiguring all volumetric variations into meaningful transitions, which can be exploited to detect and classify AD patterns.

Let a function $\boldsymbol{v}$ that maps all voxels V_{AT} in G_{AT} be defined in affine transformed vector space (i_r, j_r, k_r) to a grid of (i_s, j_s, k_s) positional vectors. The first order partial derivative of $\boldsymbol{v}$ can be expressed as $\nabla \boldsymbol{v}$. The $\nabla \boldsymbol{v}$ transforms the image domain: $D^{ARS} \rightarrow D^{J}$, where D^{J} represents the Jacobian domain of sMRI. This transformation function computes $\nabla \boldsymbol{v}$ at each voxel of G_{AT} with respect to i_s, j_s and k_s. The $\nabla \boldsymbol{v}$ forms the Jacobian matrix ($\boldsymbol{J_v}$) such that $\boldsymbol{J_v} \in D^{J}$ and $\boldsymbol{J_v}$ for an arbitrary voxel I_s can be represented by Eq. (4).

$$\boldsymbol{J_v} \leftarrow \nabla \boldsymbol{v}(\boldsymbol{I}(\boldsymbol{i_s}, \boldsymbol{j_s}, \boldsymbol{k_s})) = \begin{bmatrix} \frac{\partial \boldsymbol{v}}{\partial \boldsymbol{i_s}} & \frac{\partial \boldsymbol{v}}{\partial \boldsymbol{j_s}} & \frac{\partial \boldsymbol{v}}{\partial \boldsymbol{k_s}} \end{bmatrix} \tag{4}$$

where $\boldsymbol{v}$ lies in the 3-dimensional plane, so it can be decomposed into basis functions $\boldsymbol{v} = v_{i_r}\hat{i} + v_{j_r}\hat{j} + v_{k_r}\hat{k}$, where $\hat{i}$, $\hat{j}$ and $\hat{k}$ are the unit vectors along x, y and z directions. The determinant of $\boldsymbol{J_v}$ can be computed using Eq. (5).

$$|\boldsymbol{J_v}| = \begin{vmatrix} \frac{\partial v_{i_r}}{\partial \boldsymbol{i_s}} & \frac{\partial v_{i_r}}{\partial \boldsymbol{j_s}} & \frac{\partial v_{i_r}}{\partial \boldsymbol{k_s}} \\ \frac{\partial v_{j_r}}{\partial \boldsymbol{i_s}} & \frac{\partial v_{j_r}}{\partial \boldsymbol{j_s}} & \frac{\partial v_{j_r}}{\partial \boldsymbol{k_s}} \\ \frac{\partial v_{k_r}}{\partial \boldsymbol{i_s}} & \frac{\partial v_{k_r}}{\partial \boldsymbol{j_s}} & \frac{\partial v_{k_r}}{\partial \boldsymbol{k_s}} \end{vmatrix} \tag{5}$$

The $|\boldsymbol{J_v}|$ in (5) is called a Jacobian map for an arbitrary voxel I_s and is a quantitative factor to record the type of deformations D_T incorporated by the image registration step. The value of D_T indicates the type of volumetric transition as illustrated in Eq. (6).

$$\boldsymbol{D_T} = \begin{cases} \textit{volume compression if } |\boldsymbol{J_v}| < 1; \\ \textit{volume expansion if } |\boldsymbol{J_v}| > 1; \\ \textit{no change if } |\boldsymbol{J_v}| = 1. \end{cases} \tag{6}$$

The value of $\boldsymbol{D_T}$ identifies the brain's volume change at voxel level and provides the main reason of employing JD features. The first two conditions of Eq. (6) indicate the compression and expansion of a single voxel volume respectively, while the third condition triggers when $|\boldsymbol{J_v}|$ stays unity and in return highlights the fact that there is no change in the voxel volume. The total number of $|\boldsymbol{J_v}|$ in a single brain image are equal to the total number of voxels available in it. Each voxel in $\boldsymbol{G_{AT}}$ is replaced with its corresponding $|\boldsymbol{J_v}|$ to form $\boldsymbol{J_f}$. The three conditions listed in Eq. (6) play a major role in developing a high-performance CNN-based classifier. The computation of $\boldsymbol{J_f}$ is a linear process and does not change the dimensions of the image. Hence, the dimensions of the sMRI after JD conversion are identical to the AT image (i.e. $181 \times 217 \times 181$). As an example, the effect of JD transformation for an arbitrary AD patient is illustrated in Fig. 5, where Fig. 5(a) and Fig. 5(b) represent the AT image in SD and its corresponding JD transformed version respectively. Fig. 5(b) illustrates voxels which strictly follow the condition $|\boldsymbol{J_v}| \neq 1$. We exclude voxels that satisfy the $|\boldsymbol{J_v}| = 1$ condition, because we want to highlight the brain regions which have undergone localized volumetric change and avoid predominant voxels which remain volumetrically unchanged for pictorial representation. This is only for the sake of illustration, while no voxel filtration is performed during the training stage of the proposed classifier. Fig. 5(b) shows the voxel level volume changes captured by JD transformation where the hippocampus region exhibits higher changes in volumetric density compared to the other regions. The findings are consistent with the fact that hippocampus is one of the major brain regions that is prominently more affected by the progression of AD [35].

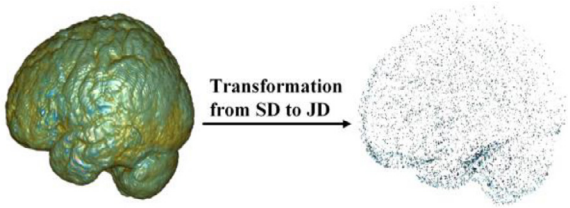

(a) AT image (b) JD image

Fig. 5. Illustration of an arbitrary sMRI transformation from spatial domain (SD) to Jacobian domain (JD). JD captures structural changes associated with the AD patterns. (a) Affine transformed (AT) image in SD (b) JD image exhibiting voxels which strictly follow the conditions $|\boldsymbol{J_v}| \neq 1$.

A comparison of the percentage voxel count between AD and HC classes is performed to differentiate the group differences generated by performing Jacobian transformation for all dataset sMRIs. First, the voxel values of all images corresponding to AD ($\boldsymbol{I_{AD}}$) as well as HC ($\boldsymbol{I_{HC}}$) are counted and collected into two groups and then these $\boldsymbol{I_{AD}}$ and $\boldsymbol{I_{HC}}$ are further sub-categorized on the basis of whether the value of $|\boldsymbol{J_v}|$ for each voxel is unity or not. Finally, these values are converted to percentages for a fair group comparison as plotted in Fig. 6(a). The stacked bar graph in Fig. 6(a) is divided into two sub-categories based on the value of $|\boldsymbol{J_v}|$. The percentage count in the sub-category of $|\boldsymbol{J_v}| = 1$ indicates voxel-wise volumetric brain regions which have not been changed after JD transformation, while $|\boldsymbol{J_v}| \neq 1$ indicates those brain regions which have undergone structural changes. The AD bar indicates that there are 0.4% voxels in the sub-category of $|\boldsymbol{J_v}| \neq 1$ compared to 0.19% in the corresponding HC category. This means that there is more than twice the number of localized volumetric changes in AD affected brain images in comparison to its counterpart. Similarly, Fig. 6(a) shows the percentage voxel count where $|\boldsymbol{J_v}| = 1$ for both AD and HC classes, which are 99.60% and 99.81% respectively.

The distribution of the JD voxel count for $|\boldsymbol{J_v}| = 1$ and its converse is calculated and plotted in Fig. 6(b)~(c). It can be observed from Fig. 6(b) that there are fewer voxels for the AD class at $|\boldsymbol{J_v}| = 1$. This indicates the existence of fewer voxels in AD that show no volumetric change compared to HC, whereas Fig. 6(c) shows that there is a higher number of voxels for AD in comparison to HC at $|\boldsymbol{J_v}| \neq 1$, which means there are many more voxels that exhibit localized volumetric changes in AD while their count is lower in

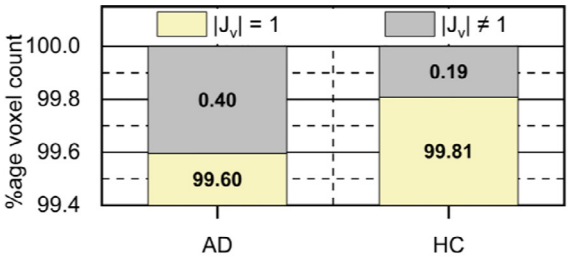

(a) Groupwise percentage voxel count.

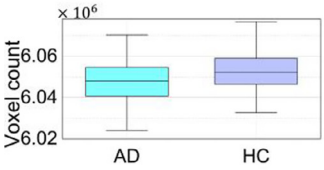

(b) $|\boldsymbol{J}_v| = 1$.

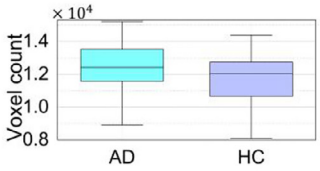

(c) $|\boldsymbol{J}_v| \neq 1$.

Fig. 6. Comparison of group differences generated between AD and HC groups after Jacobian transformation. (a) Percentage voxel count. (b)∼(c) Distribution of voxel count for $|\boldsymbol{J}_v| = 1$ and $|\boldsymbol{J}_v| \neq 1$ respectively.

HC. We removed voxels that have a '0′ value before and after JD transformation to remove a fixed bias from the statistical comparisons presented in Fig. 6. These results reinforce the fact that the JD transformation captures localized volumetric transitions associated with AD brain structure and consequently reveals the brain atrophic patterns for disease classification.

All CNN-based classifiers implement convolutional layers, which convolve the input image (i.e., matrix) with a suitable kernel. The convolution sum of an image with a zero spatial frequency turns out to be a meaningless result and if the kernel mask is similar to the one normally used for image sharping, then the convolution sum turns out to be absolutely zero. In our scenario, all such voxel-sized brain regions with no transitions in volumetric brain structure yield $|\boldsymbol{J}_v| = 1$ in JD transformed images. When these JD domain images are fed to the CNN classifier, then the meaningless features from all such regions are effectively filtered out. This enables the employed CNN classifier to focus only on those brain structures within the sMRI which have been altered due to the development of AD and eventually classifies the subjects with a high classification performance.

4.2. Implementation

The proposed algorithm is implemented using a computer with a GPU (i.e. NVIDIA GeForce RTX 2080 Ti 12GB GDDR6) and a 64-bit AMD Ryzen Threadripper 1900 × 8-Core processor with installed RAM size of 64GB DDR4. The implementation is performed in the Python-based Keras library. The RMSprop optimizer is used for training the neural network and the binary cross-entropy class is employed as the loss function, which is defined in Eq. (7).

$$\mathcal{L}(\boldsymbol{W}) = -\frac{1}{\boldsymbol{N}} \sum_{\boldsymbol{n}=1}^{\boldsymbol{N}} \log\left(\mathcal{P}\left(\hat{\boldsymbol{y}}_{\boldsymbol{n}} \mid \boldsymbol{X}_{\boldsymbol{n}}; \boldsymbol{W}\right)\right), \tag{7}$$

where N is the total number of images and $\hat{y}_n$ is the predicted class label of a given subject X_n for the training set $\{(X_n,\ y_n)\}_{n=1}^{N}$, while $\mathcal{P}(\hat{y}_n \mid X_n;\ \boldsymbol{W})$ is the probability of correct prediction for the X_n. The total trainable parameters for the model are 769,106 and a mini-batch size of 2 is selected. The proposed model is trained and validated on a set of 160 and 40 images respectively. The objective of the training stage is to reduce the value of the binary cross-entropy loss function, which eventually improves the training and validation accuracy. At the end of the training session, the model is applied to a set of validation images to evaluate the classification performance of the proposed algorithm.

4.3. Proposed architecture

The proposed architecture utilizes the *Sequential* model available in the Keras library, consisting of an input, three convolutional, three max-pooling, a flattened, a fully connected and an output layer/s. The intuition of purposing a mixed neural network architecture comes from LeNet-5 structure [36], which consists of hidden as well as fully connected layers and may be effective in identifying AD patterns. The number of layers is chosen in terms of validation performance. The proposed architecture is shown in Fig. 7. The size of the input image is $181 \times 217 \times 181$ voxels. A rectified linear unit (reLU) is used as an activation function during all operations involved in the convolution layers, no padding function is used to compute the convolutional sum, and this produces a slight change in the output shape of every convolutional layer. Each convolutional layer is strengthened with an l_2-norm kernel regularizer (KR) to avoid overfitting the classification model by applying a penalty on the layer's kernel. The first convolutional layer employs a kernel size of $3 \times 3 \times 3$ voxels with a filter dimension of 16, KR factor of 10^{-3} and its output shape is $179 \times 215 \times 176 \times 16$. The output from the first convolution layer is fed to the first max-pooling layer which utilizes a kernel size of $3 \times 3 \times 3$ units for reshaping the MRI data to $59 \times 71 \times 59 \times 16$. This downsampled version is inputted to the second convolutional layer, which utilizes a kernel size of $5 \times 5 \times 5$ units with a size of 32 output filters, KR factor of 10^{-4} and its output shape is $55 \times 67 \times 55 \times 32$. The output of the second convolution layer is sent to the second max-pooling layer with a kernel size of $4 \times 4 \times 4$ units, which downsamples the MRI data again to produce an output shape of $13 \times 16 \times 13 \times 32$. The output from the second max-pooling layer is sent to the third and last 3D convolutional layer, which employs a kernel size of $7 \times 7 \times 7$ units, KR factor of 10^{-5} and filters of 64 dimensions, while the output shape of the third con-

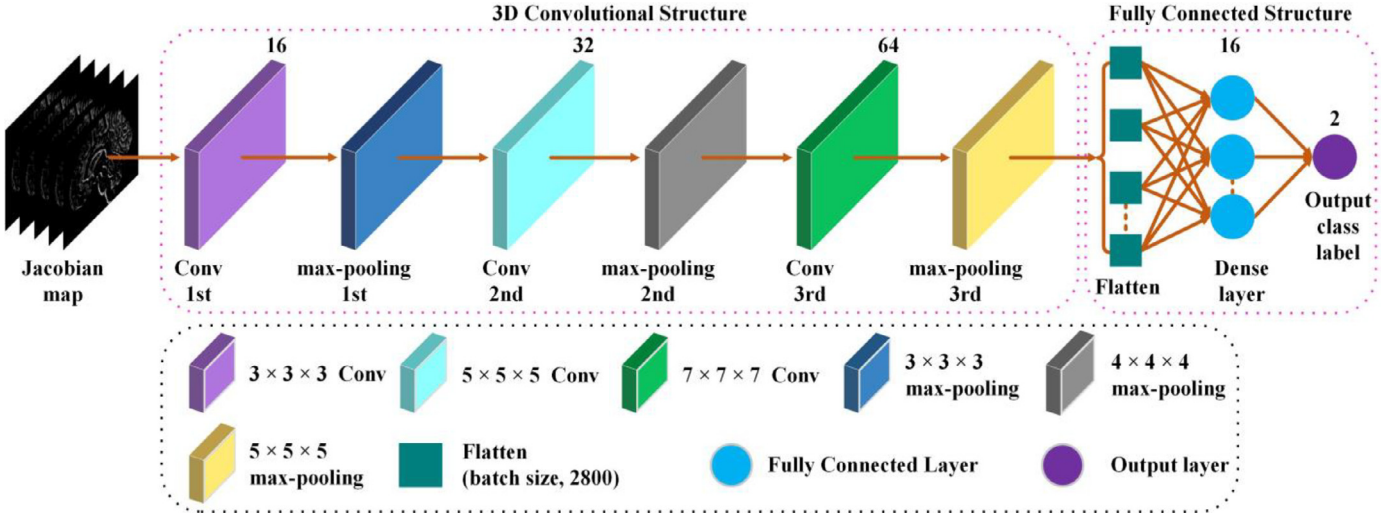

Fig. 7. Illustration of JD-CNN architecture for AD/HC classification. The architecture consists of two parts (i) 3D CNN layers (ii) 1D fully connected layers.

volutional layer reduces to $7 \times 10 \times 7 \times 64$. This output is eventually pushed to the last 3D max-pooling layer with a kernel size of $5 \times 5 \times 5$ units, which downsamples the MRI data further and after a successful max-pooling operation, its output shape becomes $1 \times 2 \times 1 \times 64$. In order to incorporate the fully connected dense layers in the proposed architecture, it is necessary to utilize a flattened layer to convert four-dimensional MRI data to a one-dimensional shape, so that it can be fed to a dense layer, which is ultimately used for classification purposes. Hence, a flattened layer is placed after the third max-pooling layer and it flattens the MRI data to a one-dimensional space with output dimensions of 128 units. Subsequently, this flattened layer is fully connected to the dense layer, and it consists of 16 units. In addition, like convolutional layers, this layer also utilizes the reLU activation function. The last layer of the proposed architecture is the output layer which provides a class label for each MRI image. The output shape of the dense layer is 16 units, which also suggests that the number of units utilized in the dense layer is 16. It is activated by a sigmoid function (ς) and consists of 2 units. This layer generates binary class labels as output to classify AD versus HC samples. The total number of trainable parameters in the proposed architecture is 796,106.

5. Experiment results

The experimental performance of the proposed algorithm is analyzed in this section. The algorithm's AD classification behavior is evaluated in terms of validation performance, -fold validation performance and test performance.

5.1. Evaluation parameters

The proposed model is evaluated to classify AD vs. HC subjects. The performance of the algorithm is assessed using four evaluation parameters, namely classification accuracy (ACC), sensitivity (SEN), specificity (SPE) and area under receiver operating characteristics (ROC) curve (AUC). ACC, SEN and SPE are defined by Eqs. (8), (9) and (10) respectively.

$$\boldsymbol{ACC} = \frac{\boldsymbol{T_{pos}} + \boldsymbol{T_{neg}}}{\boldsymbol{T_{pos}} + \boldsymbol{T_{neg}} + \boldsymbol{F_{pos}} + \boldsymbol{F_{neg}}} \tag{8}$$

$$\boldsymbol{SEN} = \frac{\boldsymbol{T_{pos}}}{\boldsymbol{T_{pos}} + \boldsymbol{F_{neg}}} \tag{9}$$

$$\boldsymbol{SPE} = \frac{\boldsymbol{T_{neg}}}{\boldsymbol{T_{neg}} + \boldsymbol{F_{pos}}} \tag{10}$$

where T_{pos}, T_{neg}, F_{pos} and F_{neg} represent true positive, true negative, false positive and false negative respectively. To compute AUC, we first identify all possible pairs of SEN and 1-SPE by changing the discretizing threshold, which is applied on the classification scores. The total number of thresholds is 200.

5.2. Analysis pertaining to validation performance

The validation performance of the proposed JD-CNN algorithm is computed by varying the learning rate (LR) from 10^{-6} to 55×10^{-4} with an increment of 5×10^{-4} and the corresponding performances are shown in Fig. 8(a) ~Fig. 8(m) respectively. The validation performance corresponding to each LR is recorded up to 100 epochs in search of maximum values of evaluation parameters to demonstrate the optimum performance of JD-CNN. The performance points which indicate maximum values of classification accuracy are termed as best performance points (BPPs). In case there is a tie between two epochs for selection of a BPP in terms of validation ACC then the epoch with higher validation AUC is selected. The performance points which do not exhibit any change anymore and become steady are termed as stable performance points (SPPs).

The selection of suitable LR is very important to achieve an exceptional learning performance of JD-CNN because the optimization process may be confined to local minimum values if a smaller LR is selected. Similarly, a larger LR may be responsible for increasing loss values. Hence, a suitable and optimal LR value should be selected to ensure the high performance of a classifier. The BPPs corresponding to LR are identified and recorded as shown in Fig. 8. Subsequently, these BPPs are plotted against each LR as shown in Fig. 9. This plot enables us to identify and select suitable LRs to compute the optimum test performance of JD-CNN.

Fig. 9 reveals that the BPP in terms of validation ACC is achieved at LR $= 15 \times 10^{-4}$. At this LR, the validation ACC, validation AUC, validation SEN and validation SPE exhibited a high value of 97.96, 98.96, 98.96, and 97.92 respectively. In the case of LR $= 15 \times 10^{-4}$, the BPP is achieved at epoch number **18**. The model weights corresponding to this epoch are stored to evaluate the test performance. The validation ACC of the proposed JD-CNN for LR $= 15 \times 10^{-4}$ becomes steady and stable at epoch number 20 and beyond as shown in Fig. 8(d). Hence, the SPPs have a span over the epoch number 20 to 100.

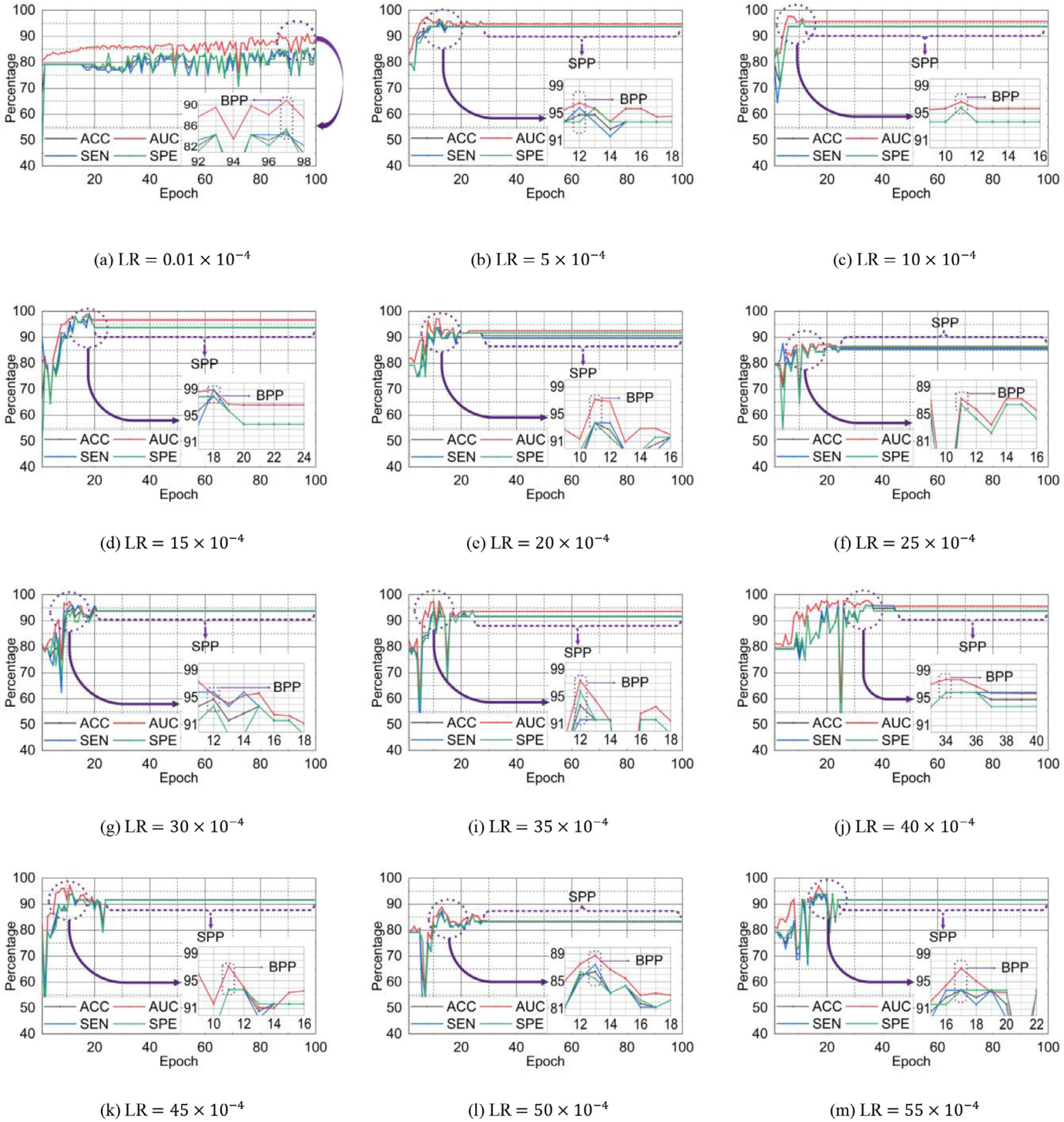

(a) LR = 0.01×10^{-4} (b) LR = 5×10^{-4} (c) LR = 10×10^{-4}

(d) LR = 15×10^{-4} (e) LR = 20×10^{-4} (f) LR = 25×10^{-4}

(g) LR = 30×10^{-4} (i) LR = 35×10^{-4} (j) LR = 40×10^{-4}

(k) LR = 45×10^{-4} (l) LR = 50×10^{-4} (m) LR = 55×10^{-4}

Fig. 8. Illustration of the proposed JD-CNN validation performance at different values of LRs. (a)∼(m) exhibit the performance by varying LR from 10^{-6} to 55×10^{-4} with an increment of 5×10^{-4} respectively. The highlighted dotted circle contains the BPP points and dotted curly braces indicates the SPP region.

5.3. Analysis pertaining to 15-fold cross-validation

The validation performance may be influenced by the selection of training, validation and testing dataset samples. The reason behind the variation in the validation performance is the involvement of variance during the dataset splitting process. To overcome the effect of variance over the performance of the proposed model, we computed 15-fold cross-validation. The 15-fold cross-validation was evaluated 100 times and then averaged the performance values to reduce the impact of random splits. The algorithm is run for 100 epochs against each fold and the performance values corresponding to the best validation ACC are stored.

Moreover, the 15-fold cross-validation was computed to identify the optimal LR by varying it from 10^{-6} to 55×10^{-4} with an increment of 5×10^{-4} as detailed in Table 2. The best 15-fold cross-validation results are achieved at LR = 15×10^{-4}, which validates our initial selection of LR during the evaluation of the validation performance given in section 5.2.

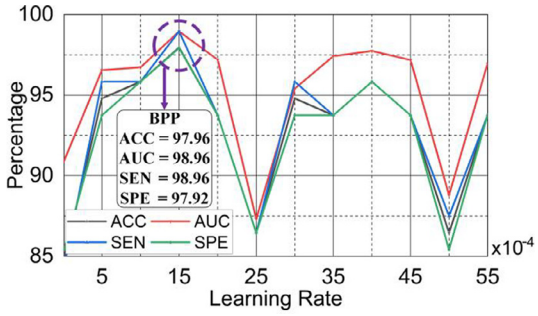

Fig. 9. Illustration of variations in validation performance with respect to learning rates. Each percentage indicates the specific epoch performance corresponding to the best validation accuracy selected among 100 epochs.

TABLE 2
15-Fold cross validation performance for sMRI data of ADNI-1 by varying learning rate (LR).

LR (10^{-4})	ACC	SEN	SPE	AUC
0.01	87.24	86.90	86.97	88.01
5	94.69	95.19	94.15	96.14
10	95.08	95.82	93.79	96.95
15	**95.42**	**96.13**	**94.17**	**97.26**
20	93.28	94.11	92.82	95.59
25	89.50	89.72	88.31	91.24
30	93.34	94.04	92.91	95.72
35	93.47	94.46	93.10	95.84
40	94.62	94.96	93.53	96.48
45	93.89	93.91	92.80	95.26
50	90.34	90.48	89.69	92.82
55	92.23	92.52	91.06	94.32

The 15-fold cross-validation ACCs are smaller than the corresponding validation ACCs depicted in Fig. 8, which are obtained from random manual dataset split into training and validation samples. The decrease in 15-fold validation ACCs suggests that there is a variance when splitting the dataset into training, validation, and testing subsets. It is also important to note that the values of the JD-CNN's 15-fold cross-validation ACCs are still reasonably high for an acceptable AD/HC classification scheme.

5.4. Effectiveness of Jacobian domain classification

The test set contains 38 samples and is separate from the training and validation sets. The algorithm is trained on the training set, and the best model is saved according to validation ACC at LR $= 15 \times 10^{-4}$. Then, the saved model is utilized to compute the performance component of the test set. The proposed JD-CNN exploits the inherited property of JD which quantifies the brain's volumetric changes in terms of shrinkage or expansiveness [8, 34]. These types of volumetric transitions are key to identifying the brain atrophy patterns behind the development of AD. This is the main reason for the superlative performance of the proposed JD-CNN against traditional CNN classifiers, which are normally trained in the spatial domain (SD). To illustrate the supremacy of the proposed JD-CNN, we remove the Jacobian determinant map generation module from the proposed framework and re-train the same CNN framework, but this time without employing JD features and denote this implementation as SD-CNN.

The dual attention multi-instance deep learning for the AD diagnosis framework [7] and hierarchical fully convolutional network [20] were reproduced for direct comparison purposes. The size of each patch was selected as $25 \times 25 \times 25$ voxels for both these studies. The test performance of Zhu et al. [7], Lian et al. [20], SD-CNN and JD-CNN is compared and illustrated in Table 3. It is evident from Table 3 that all four performance parameters prove the superiority of JD-CNN over the competing classifiers. Even though the work of Zhu et al. [7] is not an end-to-end unified framework and requires the identification of patch location proposals separately, its classification is not superior to JD-CNN.

6. Discussion

In this paper, we proposed a novel three-dimensional Jacobean domain convolutional neural network (JD-CNN) to diagnose AD subjects. In comparison with other previously reported CNN-based AD/HC classification frameworks, reported in Table 4, which utilize spatial domain images as input to train the classifier, our proposed JD-CNN algorithm utilizes CNN architecture in the Jacobian domain and provides a quantitative measure for localized volume change. The localized volume change is one of the quantification parameters for diagnosing AD [40]. Unlike the conventional classification frameworks, which only depend on convolutional network [7, 20, 22, 35] the JD-CNN exploits the inherent property of Jacobian determinant to compute voxel-level morphological statistics. These statistics alongside the convolutional network characterize the brain atrophy caused by dementia. Additionally, different form existing AD classifiers [18, 21], the JD-CNN is basically a whole brain subject-level classifier and does not necessitate feature extraction requirements from any explicit pre-determined informative brain region or patch. This is specifically handy in practice to simplify the CAD process. This fusion of the Jacobian determinant map with deep learning results in a strong classifier that classifies the disease samples and has evaluation parameters with high values.

We have briefly summarized previously reported state-of-the art studies for AD diagnosis in Table 5. This comparison employs a different number of subjects and the selection criteria for the inclusion of specific images is diverse. In addition, not all algorithms use identical subjects and the selected number of training, validation and testing subsets varies as well [19]. Due to the aforementioned obstacles, Liu et al. [17] and Lian et al. [20] also compared their frameworks with a different number of subjects. Consequently, a similar comparative methodology is adopted for a rough comparison. A rough comparison of JD-CNN with the state-of-the-art schemes reported in Table 5 shows that our proposed JD-CNN scheme achieves a superior classification performance.

We exploited baseline T1-weighted ADNI-1 sMRIs for training, validation and testing of classification frameworks reported in Table 3. To further investigate the generalization ability of the JD-CNN, we acquired additional sMRI samples from the baseline ADNI-2 datasets that satisfied the same three data selection conditions, which were described for ADNI-1 in the section 3.1. We performed 15-fold cross-validation to develop comparative study for

TABLE 3
Direct performance comparison using sMRI data of ADNI-1 for AD classification.

Reference	Methodology	Sample size (HC + AD)	ACC	SEN	SPE	AUC
SD-CNN	Spatial domain-based CNN	154+84	87.92	90.64	85.49	88.92
Lian et al. [20]	Hierarchical CNN	154+84	90.76	89.24	92.81	94.32
Zhu et al. [7]	Attention-based CNN	154+84	94.54	93.97	95.16	96.27
JD-CNN	Jacobian map feed CNN	154+84	**96.61**	**97.83**	**95.92**	**98.34**

TABLE 4
a brief description of the previously reported state-of-the-art algorithms using smri data of adni for ad classification.

Reference	Methodology	Sample size (HC + AD)	ACC	SEN	SPE	AUC
Liu et al. [21]	Landmark based CNN	404+452	78.34	47.37	83.26	79.04
Lin et al. [22]	Patch based extreme learning machine	229+188	79.90	84.00	74.80	86.10
Li et al. [37]	Graph convolutional network	226+186	84.40	83.60	85.90	84.30
Liu et al. [35].	Hippocampus based multi-model CNN	119+97	88.90	86.60	90.80	92.50
Adeli et al. [38]	Linear discriminant analysis	101+93	92.10	–	–	94.86
Liu et al. [17]	SVM based classification	128+97	93.06	94.84	90.49	95.79
Liu et al. [39]	Multiple ensemble SVM	128+97	93.83	92.78	95.69	94.16
Chen et al. [5]	CNN integrated sparse regression	417+347	95.32	91.18	93.94	—
JD-CNN (Proposed)	Jacobian map feed CNN	154+84	**96.61**	**97.83**	**95.92**	**98.34**

TABLE 5
15-Fold cross validation performance for using sMRI data of ADNI-2.

Reference	Methodology	Sample size (HC + AD)	ACC	SEN	SPE	AUC
SD-CNN	Spatial domain-based CNN	100+94	85.96	87.72	84.21	87.90
Lian et al. [20]	Hierarchical CNN	100+94	89.91	89.04	90.79	93.44
Zhu et al. [7]	Attention-based CNN	100+94	92.63	91.96	93.30	94.67
JD-CNN	Jacobian map feed CNN	100+94	**94.20**	**94.64**	**93.75**	**96.66**

the SD-CNN, Lian et al. [20], Zhu et al. [7] and JD-CNN. A learning rate of 15×10^{-4} was selected for the SD-CNN and JD-CNN experiments. The demographic information of the 194 studied subjects from ADNI-2 is reported in Table S-III in the supplementary material, while the detailed comparative classification results are presented in Table 5. It is evident that our proposed JD-CNN classifier still outperforms the competing techniques. Moreover, the 15-fold cross-validation results of ADNI-2 are comparable with the ADNI-1 (i.e., Table 3). We can observe that the proposed classifier performed somewhat better in case of ADNI-1. The possible reason lies in the fact that the studied ADNI-2 samples have a slightly larger MMSE group difference than the ADNI-2. The classification results of additional dataset (i.e., ADNI-2) validates the generalization ability of the proposed JD-CNN in AD diagnosis.

7. Conclusion

In this paper, we proposed the transformed domain JD-CNN classification framework, exploiting the Jacobian domain in conjunction with the convolutional neural network for AD diagnosis. The proposed JD-CNN algorithm computes the whole-brain Jacobian features that identify alterations in the brain's volumetric tissues. This framework successfully overcomes the limitations of existing patch-based and ROI-based models, which lack spatially correlated awareness. Moreover, these models necessitate the correct identification and localization of the relevant patches and ROIs as well. On the other hand, the proposed JD-CNN calculates whole-brain Jacobian maps to transform the brain's volumetric variations into meaningful transitions which are then exploited to identify AD patterns and is independent of any patches and ROI extraction. To the best of our knowledge, this is the first time that the CNN has been trained in the Jacobian domain to classify AD subjects. The performance of the proposed method was evaluated on sMRI data collected from the ADNI database. The experiment results of our proposed method were compared with state-of-the-art classification algorithms, which highlighted the superior performance of JD-CNN for AD/HC classification.

Although the proposed framework demonstrated exceptional classification performance, its performance and generalization capacity may be further enhanced in the future by countering the following limitations and challenges. First, we utilized the l_2-norm kernel regularizer (KR) at each CNN layer to improve the generalization of the model. We could potentially modify our framework by introducing a network pruning strategy with the help of drop-off layers, which might further improve the generalization capability and reduce the danger of overfitting. Secondly, the utilization of JD features could be acting as a bottleneck during the network training stage, therefore, it is imperative to compute the JD features in a data-driven manner by combining the generator of JD features and the network into a unified framework. Thirdly, in our current methodology, the generated JD map may also contain changes associated with differences in registration, i.e., due to shearing and scaling operations. It may be a promising direction to further develop a module which quantitatively estimates and eradicates such differences. Fourth, we only employ sMRI modality for AD diagnosis, while disregarding the enormous advantages gained by a multimodal study, such as combining sMRI and PET images. In the future, we may investigate the performance of such a multimodal framework. Fifth, we have not considered numerous confounding factors (e.g., gender, age, education, and clinical scores) of the studied subjects. As future work, we may exploit these confounding factors to develop a joint learning classifier. Moreover, further studies may utilize the concept of transfer learning to predict subjects suffering from mild cognitive impairment and prodromal AD stages by employing the gains of the proposed JD-CNN classifier.

Declaration of Competing Interest

We have no conflicts of interest to disclose.

Data availability

Data will be made available on request.

Supplementary materials

Supplementary material associated with this article can be found, in the online version, at doi:10.1016/j.patcog.2022.109031.

References

[1] A. s. Association, 2019 Alzheimer's disease facts and figures, Alzheimer's Dementia 15 (3) (2019) 321–387.
[2] B. Lei, et al., Deep and joint learning of longitudinal data for Alzheimer's disease prediction, Pattern Recognit. 102 (2020) 107247.
[3] T. Tong, K. Gray, Q. Gao, L. Chen, D. Rueckert, A.s.D.N. Initiative, Multi-modal classification of Alzheimer's disease using nonlinear graph fusion, Pattern Recognit. 63 (2017) 171–181.
[4] J. Peng, X. Zhu, Y. Wang, L. An, D. Shen, Structured sparsity regularized multiple kernel learning for Alzheimer's disease diagnosis, Pattern Recognit. 88 (2019) 370–382.
[5] Y. Chen, Y. Xia, Iterative sparse and deep learning for accurate diagnosis of Alzheimer's disease, Pattern Recognit. 116 (2021) 107944.

[6] M.I. Razzak, S. Naz, A. Zaib, Deep learning for medical image processing: overview, challenges and the future, Classif. BioApps (2018) 323–350.
[7] W. Zhu, L. Sun, J. Huang, L. Han, D. Zhang, Dual attention multi-instance deep learning for Alzheimer's disease diagnosis with structural MRI, IEEE Trans. Med. Imaging 40 (9) (2021) 2354–2366.
[8] A.R. Ridwan, et al., Development and evaluation of a high performance T1-weighted brain template for use in studies on older adults, Hum. Brain Mapp. 42 (6) (2021) 1758–1776.
[9] A.J. Schwarz, et al., Magnetic resonance imaging measures of brain atrophy from the EXPEDITION3 trial in mild Alzheimer's disease, Alzheimer's Dementia: Transl. Res. Clin. Interv. 5 (2019) 328–337.
[10] M. Ye, et al., DeepTag: an Unsupervised Deep Learning Method for Motion Tracking on Cardiac Tagging Magnetic Resonance Images, in: Proceedings of the IEEE/CVF Conference on Computer Vision and Pattern Recognition, 2021, pp. 7261–7271.
[11] C.R. Jack Jr, et al., The Alzheimer's disease neuroimaging initiative (ADNI): MRI methods, J. Magn. Resonance Imaging:Off. J. Int. Soc. Magn. Reson. Med. 27 (4) (2008) 685–691.
[12] S. Rathore, M. Habes, M.A. Iftikhar, A. Shacklett, C. Davatzikos, A review on neuroimaging-based classification studies and associated feature extraction methods for Alzheimer's disease and its prodromal stages, Neuroimage 155 (2017) 530–548.
[13] C. Möller, et al., Alzheimer disease and behavioral variant frontotemporal dementia: automatic classification based on cortical atrophy for single-subject diagnosis, Radiology 279 (3) (2016) 838–848.
[14] C. Salvatore, A. Cerasa, P. Battista, M.C. Gilardi, A. Quattrone, I. Castiglioni, Magnetic resonance imaging biomarkers for the early diagnosis of Alzheimer's disease: a machine learning approach, Front. Neurosci. 9 (2015) 307.
[15] S. Li, et al., Abnormal changes of multidimensional surface features using multivariate pattern classification in amnestic mild cognitive impairment patients, J. Neurosci. Methods 34 (32) (2014) 10541–10553.
[16] H. Park, J.-j. Yang, J. Seo, J.-m. Lee, Dimensionality reduced cortical features and their use in the classification of Alzheimer's disease and mild cognitive impairment, Neurosci. Lett. 529 (2) (2012) 123–127.
[17] M. Liu, D. Zhang, D. Shen, Relationship induced multi-template learning for diagnosis of Alzheimer's disease and mild cognitive impairment, IEEE Trans. Med. Imaging 35 (6) (2016) 1463–1474.
[18] M. Liu, J. Zhang, E. Adeli, D. Shen, Joint classification and regression via deep multi-task multi-channel learning for Alzheimer's disease diagnosis, IEEE Trans. Biomed. Eng. 66 (5) (2019) 1195–1206.
[19] J. Wen, et al., Convolutional Neural Networks for Classification of Alzheimer's Disease: overview and Reproducible Evaluation, Med. Image Anal. (2020) 101694.
[20] C. Lian, M. Liu, J. Zhang, D. Shen, Hierarchical fully convolutional network for joint atrophy localization and Alzheimer's disease diagnosis using structural MRI, IEEE Trans. Pattern Anal. Mach. Intell. 42 (4) (2020) 880–893.
[21] M. Liu, J. Zhang, E. Adeli, D. Shen, Landmark-based deep multi-instance learning for brain disease diagnosis, Med. Image Anal. 43 (2018) 157–168.
[22] W. Lin, et al., Convolutional neural networks-based MRI image analysis for the Alzheimer's disease prediction from mild cognitive impairment, Front. Neurosci. 12 (2018) 777.
[23] H. Wang, et al., Ensemble of 3D densely connected convolutional network for diagnosis of mild cognitive impairment and Alzheimer's disease, Neurocomputing 333 (2019) 145–156.
[24] S. Basaia, et al., Automated classification of Alzheimer's disease and mild cognitive impairment using a single MRI and deep neural networks, Neuroimage Clin 21 (2019) 101645.
[25] C. Lian, M. Liu, L. Wang, D. Shen, Multi-task weakly-supervised attention network for dementia status estimation with structural mri, IEEE Trans. Neural Netw Learn Syst (2021).
[26] K. Gorgolewski, et al., Nipype: a flexible, lightweight and extensible neuroimaging data processing framework in python, Front. Neuroinform. 5 (2011) 13.
[27] M.M. McCormick, X. Liu, L. Ibanez, J. Jomier, C. Marion, ITK: enabling reproducible research and open science, Front. Neuroinform. 8 (2014) 13.
[28] B.B. Avants, N. Tustison, G. Song, Advanced normalization tools (ANTS), Insight J 2 (365) (2009) 1–35.
[29] B.A. Ardekani, J. Kershaw, M. Braun, I. Kanuo, Automatic detection of the mid-sagittal plane in 3-D brain images, IEEE Trans. Med. Imaging 16 (6) (1997) 947–952.
[30] B.A. Ardekani, A.H. Bachman, Model-based automatic detection of the anterior and posterior commissures on MRI scans, Neuroimage 46 (3) (2009) 677–682.
[31] T. Rohlfing, N.M. Zahr, E.V. Sullivan, A. Pfefferbaum, The SRI24 multichannel atlas of normal adult human brain structure, Hum. Brain Mapp. 31 (5) (2010) 798–819.
[32] C.J. Holmes, R. Hoge, L. Collins, R. Woods, A.W. Toga, A.C. Evans, Enhancement of MR images using registration for signal averaging, J. Comput. Assist. Tomogr. 22 (2) (1998) 324–333.
[33] M. Stypułkowski, K. Kania, M. Zamorski, M. Zięba, T. Trzciński, J. Chorowski, Representing point clouds with generative conditional invertible flow networks, Pattern Recognit. Lett. 150 (2021) 26–32.
[34] S. Spasov, L. Passamonti, A. Duggento, P. Lio, N. Toschi, A.s.D.N. Initiative, A parameter-efficient deep learning approach to predict conversion from mild cognitive impairment to Alzheimer's disease, Neuroimage 189 (2019) 276–287.
[35] M. Liu, et al., A multi-model deep convolutional neural network for automatic hippocampus segmentation and classification in Alzheimer's disease, Neuroimage 208 (2020) 116459.
[36] Y. LeCun, L. Bottou, Y. Bengio, P. Haffner, Gradient-based learning applied to document recognition, Proc. IEEE 86 (11) (1998) 2278–2324.
[37] H. Li, X. Shi, X. Zhu, S. Wang, Z. Zhang, FSNet: dual Interpretable Graph Convolutional Network for Alzheimer's Disease Analysis, IEEE Trans. Emerg. Top. Comput. Intell. (2022).
[38] E. Adeli, et al., Semi-supervised discriminative classification robust to sample-outliers and feature-noises, IEEE Trans. Pattern Anal. Mach. Intell. 41 (2) (2018) 515–522.
[39] M. Liu, D. Zhang, E. Adeli, D. Shen, Inherent structure-based multiview learning with multitemplate feature representation for Alzheimer's disease diagnosis, IEEE Trans. Biomed. Eng. 63 (7) (2015) 1473–1482.
[40] C.M. Fiford, et al., Patterns of progressive atrophy vary with age in Alzheimer's disease patients, Neurobiol. Aging 63 (2018) 22–32.

Syed Qasim Abbas received his MS degree in Electrical Engineering from HITEC University, Taxila Pakistan in 2016. He is currently pursuing the Ph.D. degree with the Department of Computer Science and Information Technology, La Trobe University, Melbourne, Australia. His current research include computational neuroimaging through deep learning and cryptographic image hashing.

Lianhua Chi received the dual Ph.D. degrees in computer science from the University of Technology Sydney, Australia, and the Huazhong University of Science and Technology, Wuhan, China, in 2015. She was a Post-Doctoral Research Scientist in IBM Research Melbourne. Dr. Chi was a recipient of the Best Paper Award in PAKDD in 2013. Currently, she is a Lecturer with the Department of Computer Science and Information Technology at La Trobe University since 2018. Her current research interests include data mining, machine learning and big data hashing.

Yi-Ping Phoebe Chen received the Ph.D. degree in computer science from the University of Queensland, Brisbane, Australia. She is a Professor and Chair with the Department of Computer Science and Information Technology, La Trobe University, Melbourne, Australia. She has published over 250 research papers, many of them appeared in top journals and conferences. Her research interests include the finding of the best solutions for mining, integrating, and analysing complex data structure and functions for scientific and biomedical applications.